

Optimization of Parameters Used in Algorithms of Ion-Mobility Calculation for Conformational Analyses

Chi-Kit Siu

Department of Biology and Chemistry, City University of Hong Kong, 83 Tat Chee Avenue, Kowloon Tong, Hong Kong, China

Yuzhu Guo, Irine S. Saminathan, Alan C. Hopkinson, and K. W. Michael Siu*

Department of Chemistry and Centre for Research in Mass Spectrometry, York University, 4700 Keele Street, Toronto M3J 1P3, Canada

Received: November 15, 2009

Structural information of gaseous ions can be obtained by comparing their collision cross sections as determined by ion-mobility experiments with those by theoretical modeling. Three theoretical models, the projection approximation (PA), the exact hard-sphere scattering (EHSS), and the trajectory (TJ) models, have been employed to determine the theoretical cross sections of candidate geometries. The accuracy of these models is largely dependent on the empirical parameters used for ion–buffer gas interactions. Optimal empirical parameters for each model have been determined by comparing the experimental cross sections of 20 calibrant ions with their theoretical cross sections obtained by using geometries sampled by density-functional-theory-based molecular dynamics simulations. The maximum absolute deviations of the cross sections of 15.5% (PA), 20.7% (EHSS), and 11.7% (TJ) obtained from the original parameters are reduced to 5.6% (PA), 4.6% (EHSS), and 3.4% (TJ) obtained from the new optimized parameters. The root-mean-square deviations of the predicted cross sections using the new parameters from the experimental values are also drastically reduced to 2.1% (PA), 1.9% (EHSS), and 1.6% (TJ). The new parameters are verified on protonated triglycine, protonated trialanine, and doubly protonated bradykinin.

Introduction

Ion mobility is a measure of the velocity of an ion under the influence of an electric field in a drift tube filled with a neutral buffer gas.¹ Ions of different sizes and shapes will experience different extents of interaction with the buffer gas molecules and result in different mobilities. Ion-mobility spectrometry (IMS) is a technique for separating ions in the gas phase based on this phenomenon. With its high sensitivity, fast response time, and relatively low cost, IMS has become a powerful analytical tool and has been applied to a wide range of fields in industries, environmental studies, forensic sciences, security screening, biomolecular sciences, and medical applications.²

Detailed structural information can also be determined from IMS experiments with light particles as the buffer gas, typically helium atoms. Under the conditions of sufficiently low-electric field (E) and sufficiently high helium number density (ρ), a drifting ion undergoes a large number of collisions and thermalizes to the buffer gas temperature. The drift velocity (v_d) is directly proportional to E with the mobility of the ion (K) being the proportionality constant ($K = v_d/E$). K can be expressed using the Mason–Schamp equation:

$$K = \frac{3ze\sqrt{2\pi}}{16\rho} \sqrt{\frac{1}{m} + \frac{1}{M}} \frac{1}{\sqrt{k_B T} \Omega_{\text{avg}}^{(1,1)}} \quad (1)$$

where ze is the charge of the ion; m and M are the masses of the ion and He atom, respectively; T is the gas temperature;

and k_B is the Boltzmann constant. $\Omega_{\text{avg}}^{(1,1)}$ is an orientationally averaged cross section, which is the interaction between the ion and buffer gas, and thus depends on the geometry of the ion. Comparing the experimental cross section with the theoretical cross sections calculated from plausible candidate structures provides insights into the three-dimensional structures of ions, including atomic clusters,^{3–5} polyaromatic hydrocarbons,⁶ solvated ions,^{7–9} metal–organic complexes,^{10,11} polymers,^{12–16} nucleotides,^{14,17–20} oligopeptides,^{21–23} and proteins.^{24,25}

The projection approximation (PA),³ the exact hard-sphere scattering (EHSS) method,⁵ and the trajectory (TJ) simulation⁴ are three commonly used theoretical models for calculating the cross section of a given geometry or ion structure. These models all rely on some parameters that are empirically optimized by comparing the experimental and theoretical cross sections of calibrant ions with well-characterized structures. The values of the optimized empirical parameters are influenced by the level of theory used for geometry optimization. Molecular mechanics with an empirical force field or semiempirical methods have been common choices because of their low computational cost, although the accuracies of the structural details are debatable. With the rapid development of computer technologies, density functional theory (DFT)-based geometric optimizations are now becoming a viable method to more accurately predict molecular structures. Recently, we have employed DFT methods coupled with molecular dynamics (MD) simulations to sample low-lying structures for comparison with IMS results.¹¹ In this current study, we will optimize a set of parameters for each algorithm selected for theoretical cross

* Corresponding author. Tel: (416)650-8021. Fax: (416)736-5936. E-mail: kwmsiu@yorku.ca.

section calculations, using the geometries of a variety of calibrant ions sampled by DFT-MD simulations.

Density Functional Theory—Molecular Dynamics Simulations. In ion-mobility experiments, low-lying conformers of a molecular ion are interconvertible and their populations are equilibrated in a thermal bath at a finite temperature T (T is around 298 K in typical ion-mobility instruments). This conformational dynamics is likely more important for molecular ions having flexible structures than those with more rigid structures. The dynamic structures of molecular ions are examined here using DFT-MD methods. Twenty calibrant ions were selected, including tetraalkylammonium ions $\text{TAA-}n$ $[\text{N}(\text{C}_n\text{H}_{2n+1})_4]^+$ ($n = 1-8$), protonated cyclic-dipeptides $[\text{cXxxXxx} + \text{H}]^+$ ($\text{Xxx} = \text{Gly, Ala, Ser, and Val}$) and $[\text{cYyyPro}]^+$ ($\text{Yyy} = \text{Ala and Val}$), protonated glycine $[\text{Gly} + \text{H}]^+$ and alanine $[\text{Ala} + \text{H}]^+$, benzene radical cation $[\text{C}_6\text{H}_6]^+$, naphthalene radical cation $[\text{C}_{10}\text{H}_8]^+$, iron(III) protoporphyrin IX [hemin] $^+$, and iron(III) tetraphenylporphyrin ion $[\text{TPP-Fe(III)}]^+$.

Density functional theory—molecular dynamics (DFT-MD) simulations were carried out using the VASP program (Vienna Ab initio Simulation Package).^{26–29} Local density approximation with the Perdew–Burke–Ernzerhof (PBE) gradient approximation was used for the exchange–correlation functional.³⁰ The spin-unpolarized method was used for all closed-shell protonated systems and the spin-polarized method was used for all open-shell systems: $[\text{C}_6\text{H}_6]^+$, $[\text{C}_{10}\text{H}_8]^+$, [hemin] $^+$, and $[\text{TPP-Fe(III)}]^+$. Optimized pseudopotentials for all atoms were constructed by means of the projector augmented wave (PAW) method.³¹ The electronic wave functions were described by a plane-wave basis set, with the cutoff energy (PW- E_{cutoff}) being 283 eV; these were solved by minimizing the total electronic energy at each MD time step by residual minimization—direct inversion in the iterative subspace (RMM-DIIS). To reduce the interaction between the periodical images imposed by the plane-wave basis set, an ion was put in a cubic simulation box with a large dimension (at least 7 Å between the periodic images). The DFT-MD simulations on the Born–Oppenheimer potential-energy surface were performed by solving the Newtonian equations of motion with an integration time step of 0.5 fs (a smaller time step of 0.3 fs was used for [hemin] $^+$ and $[\text{TPP-Fe(III)}]^+$ to maintain stable wave function optimization of each MD step). The ion was first heated to 298 K for a short duration (~ 0.2 ps) by rescaling the atomic velocities at every MD time step. The MD simulation was then continued with the temperature being kept at 298 K by means of a Nosé–Hoover thermostat.³²

Ion-Mobility Calculations. The algorithms used for ion-mobility calculations in this study are MOBCAL³³ and EHSS-rot.³⁴ The algorithms seek the cross section $\Omega_{\text{avg}}^{(1,1)}$ which is related to the scattering angles χ between the ion and He atoms and is obtained by integrating the momentum transfer cross section over the relative velocities g and the impact parameter b for all possible ion orientations defined by the three angles θ , ϕ , and γ :

$$\Omega_{\text{avg}}^{(1,1)} = \frac{1}{8\pi^2} \int_0^{2\pi} d\theta \int_0^\pi d\phi \sin \phi \int_0^{2\pi} d\gamma \frac{\pi}{8} \left(\frac{\mu}{k_B T} \right)^3 \times \int_0^\infty dg e^{-\mu g^2/(2k_B T)} g^5 \int_0^\infty db 2b(1 - \cos \chi(\theta, \phi, \gamma, g, b)) \quad (2)$$

where μ is the reduced mass. Equation 2 can be calculated by numerical integration of the trajectory between the He atom and the molecular ion propagated in an intermolecular potential V :

$$V(\theta, \phi, \gamma, b, r) = \sum_i^n 4\epsilon_i \left[\left(\frac{\sigma_i}{r_i} \right)^{12} - \left(\frac{\sigma_i}{r_i} \right)^6 \right] - \frac{\alpha (ze)^2}{2(n)} \left[\left(\sum_i^n \frac{x_i}{r_i^3} \right)^2 + \left(\sum_i^n \frac{y_i}{r_i^3} \right)^2 + \left(\sum_i^n \frac{z_i}{r_i^3} \right)^2 \right] \quad (3)$$

The first term is a sum of Lennard-Jones (6-12) potential between a He gas atom and individual atom i in the molecular ion. The Lennard-Jones parameters, ϵ_i (depth) and σ_i (distance), are obtained by fitting measured mobilities as a function of temperature. The second term is the charge–induced dipole interaction with α being the polarizability of He and x_i , y_i , z_i , and r_i give the relative position of each individual atom i . The trajectory model provides accurate prediction for the cross section of a given candidate geometry, but is computationally expensive.

A common, computationally efficient, approximation for eq 2 is to assume that the individual atoms in the molecular ion and He atom are hard spheres. Equation 2 is thus approximated by the orientationally averaged hard-sphere cross section Ω :

$$\Omega = \frac{1}{4\pi} \int_0^\pi d\phi \sin \phi \int_0^{2\pi} d\gamma \Omega_{\text{dir}}(\phi, \gamma) \quad (4)$$

where $\Omega_{\text{dir}}(\phi, \gamma)$ is a directional cross section. For the simplest projection approximation (PA) model, $\Omega_{\text{dir}}(\phi, \gamma)$ is calculated by projecting the molecular ion onto the yz -plane:

$$\Omega_{\text{dir}}(\phi, \gamma) = \int_{-\infty}^{+\infty} \int_{-\infty}^{+\infty} M(\phi, \gamma, y, z) dy dz \quad (5)$$

where M is unity when a collision occurs. Ω is then obtained using Monte Carlo integration by counting the number of collisions out of N numbers of He atoms randomly generated in a rectangle with an area A bracketing the projected molecular ion on the yz -plane.

It has been shown that the PA model is inadequate for calculating the cross sections of molecular ions with a concave surface on which a buffer gas atom can experience multiple collisions. This effect can be accounted for by the exact hard-spheres scattering (EHSS) model in which eq 5 (of the PA model) is replaced by

$$\Omega_{\text{dir}}(\phi, \gamma) = \int_{-\infty}^{+\infty} \int_{-\infty}^{+\infty} [1 - \cos \chi(\phi, \gamma, y, z)] dy dz \quad (6)$$

where χ is the scattering angle of the He atom.

For the PA and EHSS models, a successful collision is defined when the coordinates of the colliding He atom is within the projected area of any individual atom (X) having a collisional radius of $R(\text{X-He})$, which is the empirical parameter fitted by comparing experimental and calculated cross sections of molecular ions with known, calibrant structures.

Ion-Mobility Experiments. Ions were generated from their respective solutions by means of pneumatically assisted electrospray at a typical flow rate of 2 $\mu\text{L}/\text{min}$. The ion-mobility cell is functionally the second quadrupole (q2) of a custom-built triple-quadrupole mass spectrometer, using mostly components from a commercially available API 3000 triple-quadrupole mass spectrometer (MDS SCIEX). The instrumentation has been described in detail elsewhere.^{35,36} Briefly, the Q1 and Q3 are conventional MS analyzers; the q2 is a 20-segment quadrupole/ion-mobility cell. Ion injection into q2 was synchronized with detection, with the arrival times being recorded using a multichannel scaler. Typical ion-mobility measurements were conducted with an axial field of 40–100 V per 20.2 cm in 1 Torr of helium at 298 ± 2 K, giving E/N values of ca.

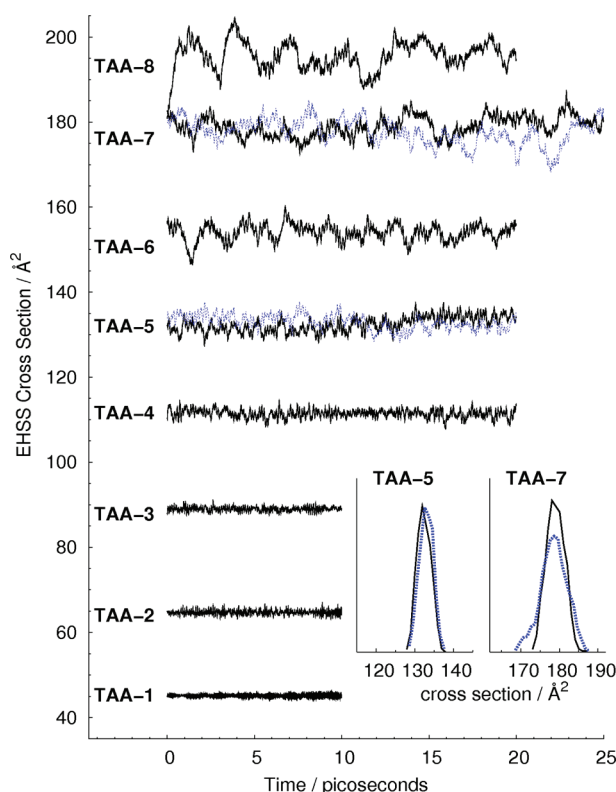


Figure 1. Evolution of the cross sections of **TAA-*n*** ($n = 1-8$) as sampled by the DFT-MD simulations. The cross sections were calculated by the EHSS model with optimal parameters ($R(\text{H-He}) = 1.50 \text{ \AA}$, $R(\text{C-He}) = 2.70 \text{ \AA}$). Two independent parallel simulations (black and blue curves) were performed for $n = 5$ and 7 and the insets show their cross-sectional distributions.

6–15 Td ($1 \text{ Td} = 10^{-17} \text{ V cm}^2$). Collision cross sections were calculated using eq 1.

Results and Discussion

Structural Sampling: Density Functional Theory Molecular Dynamics (DFT-MD). Tetraalkylammonium ions (**TAA-*n***) have low propensities for ion–ligand interactions that would lead to cluster ions and thus are good standards for calibrating ion-mobility instrumentation.³⁷ **TAA-*n***'s are singly charged ions with the cationic charge formally located at the quaternary nitrogen atom, which is covalently bound to four alkyl chains. While the structure at the central nitrogen atom of **TAA-*n*** is well-defined as being tetrahedral, there is a large degree of flexibility in each of the individual alkyl chains. This flexibility increases with increasing chain length, n , as is demonstrated by the DFT-MD simulations. Figure 1 shows evolutions of theoretical cross sections of the structures of **TAA-*n*** ($n = 1-8$) sampled by the DFT-MD simulations. The theoretical cross sections were calculated using the EHSS model with optimal parameters of $R(\text{H-He}) = 1.50 \text{ \AA}$ and $R(\text{C-He}) = 2.70 \text{ \AA}$ by means of the EHSSrot software (vide infra). As n increases, variations of the cross section are increased (Figure 1). It is also clearly reflected by the standard deviations of the cross sections, which gradually increased from 0.3 \AA^2 (for $n = 1$) to 3.3 \AA^2 (for $n = 8$) (see Table 1). For $n = 5$ and $n = 7$, two independent DFT-MD trajectories were simulated, each starting from an initial structure that differed in conformation from the other. These independent parallel runs show very similar distributions of the cross sections (inserts in Figure 1). The differences in average cross section obtained from the two

independent runs are also small, within 1 \AA^2 , for all theoretical models (Table 1). Therefore, the simulation times are sufficiently long to attain conformational equilibrations for the current studies.

DFT-MD simulations were also performed for protonated glycine [$\text{Gly} + \text{H}^+$] and alanine [$\text{Ala} + \text{H}^+$], protonated cyclic dipeptides [$\text{cXxxXxx} + \text{H}^+$] ($\text{Xxx} = \text{Gly, Ala, Ser, and Val}$) and [$\text{cYyyPro} + \text{H}^+$] ($\text{Yyy} = \text{Ala and Val}$), and planar molecular ions including [C_6H_6] $^+$, [C_{10}H_8] $^+$, tetraphenylporphyrin iron(III) [TPP-Fe(III)^+], and protoporphyrin IX iron(III) ion [hemin] $^+$. For [$\text{cYxxPro} + \text{H}^+$], two DFT-MD simulations were performed, each with protonation on different carbonyl oxygen atoms. The cross-section distributions of these compounds are narrower than those of the more flexible **TAA-*n*** with long alkyl chains ($n > 5$).

All selected molecular ions, including **TAA-*n***, have well-defined structures and are used as calibrants for optimizing the empirical parameters for theoretical cross-section calculations. Figure 2 shows comparisons between the collision cross sections measured by ion-mobility experiments and the theoretical cross sections calculated with the MOBCAL software for the TJ method and the EHSSrot software for the PA and EHSS methods. The numerical values are summarized in Table 1. The experimental values of each ion are the average obtained from a minimum of three runs, while the theoretical values are the average obtained from the DFT-MD sampled structures. The predicted cross sections from all three models show linear correlations with the experimental collision cross sections, but are consistently larger than the latter when the originally implemented empirical parameters (developed for use with molecular mechanics-derived structures) were used (Figure 2 and Table 1). The average percent difference ($\langle\% \text{ diff}\rangle$) between the cross sections predicted by the PA model and the measured values is 10.3% with a root-mean-square deviation (rmsd) of 10.9%. Using the EHSS model, by which effects of multiple scattering are included, increases the $\langle\% \text{ diff}\rangle$ to 17.5% and the rmsd to 17.5%. The TJ model also overestimates the cross sections by a $\langle\% \text{ diff}\rangle$ of 8.4% and rmsd of 8.5%. These differences are significantly larger than the typical experimental errors of 2% in IMS measurements.³ Determining the empirical parameters capable of giving more accurate predicted cross sections based on DFT-derived structures is, therefore, desirable and needed. In the following sections, attempts to develop such parameters for use with each theoretical model will be discussed.

Parameters for the Projection Approximation (PA) and the Exact Hard-Sphere Scattering (EHSS) Models. The EHSSrot software³⁴ was used to calculate the PA and EHSS cross sections. Ten runs each with 10 000 trajectories were performed (i.e., a total of 100 000 points for each DFT-MD geometry). The parameters being optimized were the collision radii (in \AA) of the H and X atoms in He as the buffer gas ($R(\text{H-He})$ and $R(\text{X-He})$, respectively), where X was C, N, or O. The $R(\text{H-He})$ and $R(\text{X-He})$ distances were varied from 1.50 to 2.20 \AA , and from 2.20 to 2.75 \AA , respectively. The cross sections of the DFT-MD sampled structures of the calibrants were then calculated at each combination of the $R(\text{H-He})$ and $R(\text{X-He})$. For [hemin] $^+$ and [TPP-Fe(III)^+], the iron(III) ion was buried at the center of the porphyrin ring. Therefore, changing the $R(\text{Fe-He})$ parameter had a negligible effect on the overall cross section and thus $R(\text{Fe-He})$ was fixed to the original parameter of 2.70 \AA .

Hydrogen atoms are mostly exposed on the surface of a molecule and have the largest probability of interacting with the colliding He atoms. Thus, $R(\text{H-He})$ presumably plays the

TABLE 1: Collision Cross Sections Obtained Experimentally by Ion-Mobility Spectrometry (IMS) and Theoretically (THEO) by the Projection Approximation (PA), the Exact Hard-Sphere Scattering (EHSS) Method, and the Trajectory (TJ) Simulations Using the Original Parameters and Optimized Parameters^c

diff > 15 %	IMS	DFT-MD												
diff > 10 %		Original parameters						Optimized parameters						
diff > 5 %		$R(\text{H-He}) = 2.20$ $R(\text{X-He}) = 2.70$				scaling factor S_{TJ} = 1.00		$R(\text{H-He}) = 2.01$ $R(\text{C-He}) = 2.35$ $R(\text{N-He}) = 2.26$ $R(\text{O-He}) = 2.26$		$R(\text{H-He}) = 1.50$ $R(\text{C-He}) = 2.70$ $R(\text{N-He}) = 2.50$ $R(\text{O-He}) = 2.50$		scaling factor S_{TJ} = 0.92		
-5 % < diff < 5 %														
-3 % < diff < 3 %														
-2 % < diff < 2 %														
diff < -5 %														
		PA ^a	SD _{PA} ^b	EHSS ^a	SD _{EHSS} ^b	TJ ^a	SD _{TJ} ^b		PA ^a	SD _{PA} ^b	EHSS ^a	SD _{EHSS} ^b	TJ ^a	SD _{TJ} ^b
TAA-1	47.3	52.2	0.4	54.0	0.5	49.9	1.0		47.1	0.4	45.2	0.3	45.9	0.4
TAA-2	64.0	71.9	0.6	75.4	0.7	68.8	1.3		65.8	0.5	64.7	0.5	63.5	0.7
TAA-3	87.0	96.2	0.5	103.8	0.7	94.3	1.6		88.7	0.5	89.0	0.5	87.4	0.8
TAA-4	109.4	118.4	1.0	129.9	1.3	118.8	2.3		109.8	1.0	111.4	1.0	110.1	1.2
TAA-5(1)	131.6	139.2	2.1	154.2	2.4	140.8	3.2		129.5	1.9	132.4	1.7	130.9	1.9
TAA-5(2)		140.2	1.9	155.1	2.2	141.6	2.9		130.4	1.7	133.0	1.7	131.8	1.8
TAA-6	153.5	161.6	2.4	179.7	2.7	163.7	3.8		150.8	2.2	154.0	2.0	152.7	2.2
TAA-7(1)	173.8	188.1	3.1	210.1	3.3	190.5	4.4		175.8	2.8	179.0	2.3	177.7	2.6
TAA-7(2)		187.9	4.7	209.6	4.9	189.8	5.0		175.6	4.2	178.5	3.4	177.1	3.6
TAA-8	194.3	204.4	4.2	228.7	4.6	208.1	5.7		191.5	3.7	195.7	3.3	194.6	3.7
[cGlyGly + H] ⁺	50.8	58.1	0.3	60.0	0.3	56.0	1.2		50.4	0.3	50.0	0.2	50.8	0.4
[cAlaAla + H] ⁺	59.8	68.2	0.5	71.4	0.6	65.9	0.6		60.4	0.5	60.7	0.5	60.5	0.6
[cSerSer + H] ⁺	64.8	74.3	0.5	77.9	0.5	72.4	0.6		65.4	0.4	66.5	0.5	66.2	0.6
[cValVal + H] ⁺	77.0	85.9	1.0	91.1	1.3	84.4	1.2		77.6	1.0	79.2	1.1	78.0	1.1
[cAlaPro + H] ⁺ (1)	66.3	74.5	0.4	78.6	0.6	72.5	0.6		66.8	0.4	66.2	0.4	66.8	0.6
[cAlaPro + H] ⁺ (2)		74.6	0.4	78.8	0.5	72.6	0.6		66.9	0.4	66.3	0.4	66.9	0.5
[cValPro + H] ⁺ (1)	74.5	83.5	0.7	88.7	0.8	82.0	0.8		75.4	0.6	75.9	0.6	75.7	0.8
[cValPro + H] ⁺ (2)		83.5	0.6	88.8	0.7	82.1	0.7		75.6	0.6	75.9	0.6	75.8	0.7
[Gly + H] ⁺	41.3	47.8	0.3	48.9	0.3	45.8	1.0		40.9	0.3	40.3	0.2	41.5	0.4
[Ala + H] ⁺	46.0	53.1	0.4	54.9	0.4	51.1	0.5		46.3	0.3	45.6	0.3	46.5	0.5
[C ₆ H ₆] ⁺⁺	43.8	50.2	0.3	51.3	0.3	47.8	0.9		44.5	0.3	43.8	0.2	43.2	0.3
[C ₁₀ H ₈] ⁺⁺	58.2	64.9	0.2	66.7	0.3	61.9	1.1		58.3	0.2	58.1	0.2	56.2	0.4
[hemin] ⁺	166.3	169.2	1.0	183.6	1.6	173.8	3.4		157.1	0.9	167.9	1.1	162.9	1.5
[TPP-Fe(III)] ⁺	187.7	190.0	0.8	210.8	1.2	197.1	3.3		177.1	0.8	189.3	0.9	184.3	1.3
< %diff >		10.3		17.5		8.4			-0.2		0.6		-0.1	
max. abs. dev.		15.5		20.7		11.7			5.6		4.6		3.4	
RMSD / %		10.9		17.5		8.5			2.1		1.9		1.6	

^a Average values of theoretical cross sections obtained from the structures sampled from DFT-MD simulations. ^b Standard deviations of theoretical cross section SD_i obtained from the structures sampled from DFT-MD simulations. ^c Percent differences % diff = $[(\Omega_{\text{THEO}} - \Omega_{\text{IMS}})/\Omega_{\text{IMS}}] \times 100\%$ and the average values of all calibrants <% diff> are expressed in different colors (as indicated by the legend).

most significant role in the overall cross section of a molecular ion. Here, $R(\text{H-He})$ and $R(\text{C-He})$ were optimized simultaneously using the calibrants, **TAA-*n***, $[\text{C}_6\text{H}_6]^{++}$, $[\text{C}_{10}\text{H}_8]^{++}$, and $[\text{TPP-Fe(III)}]^+$, in which the molecular surfaces contain only hydrogen and carbon atoms. The average percent differences between the predicted cross section Ω_{THEO} and measured cross sections Ω_{IMS} , $\langle[(\Omega_{\text{THEO}} - \Omega_{\text{IMS}})/\Omega_{\text{IMS}}] \times 100\% \rangle$, at each set of parameters are summarized in Figure 3, a and b, for the PA and EHSS models, respectively. The predicted cross section is insensitive to changes in $R(\text{C-He})$ at large $R(\text{H-He})$ (>2.0 Å), attributable to the fact that the hydrogen atoms are always located on the molecular surface. As $R(\text{H-He})$ decreases, C atoms are effectively becoming more exposed to the molecular surface; consequently the value of $R(\text{C-He})$ becomes sensitive to the predicted cross sections. The rmsd values of the percent differences between predicted and measured cross sections are shown in Figure 3, c and d, from which the minima (valleys) determine the optimal parameters, that is, $(R(\text{H-He})/\text{Å}, R(\text{C-He})/\text{Å}) = (2.01, 2.35)$ for the PA model and $(1.50, 2.70)$ for the EHSS model, respectively. A full list of numerical data obtained from the models using different parameters is available in the

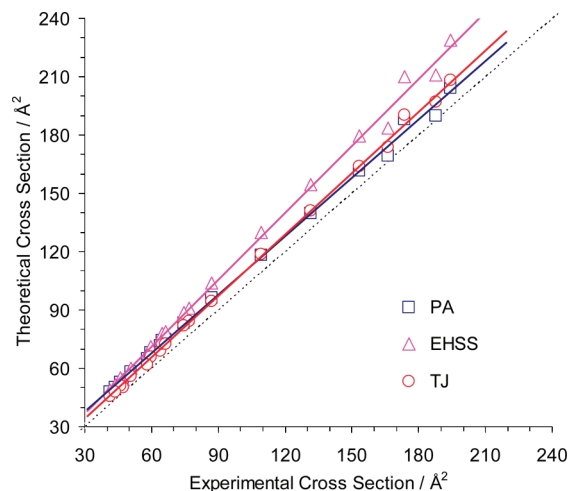


Figure 2. Comparisons between the collision cross sections measured by ion-mobility experiments and the theoretical cross sections calculated by the PA, EHSS, and TJ models, using the original parameters for all calibrants. The black dotted line indicates a perfect match between experimental and theoretical values (i.e., slope = 1).

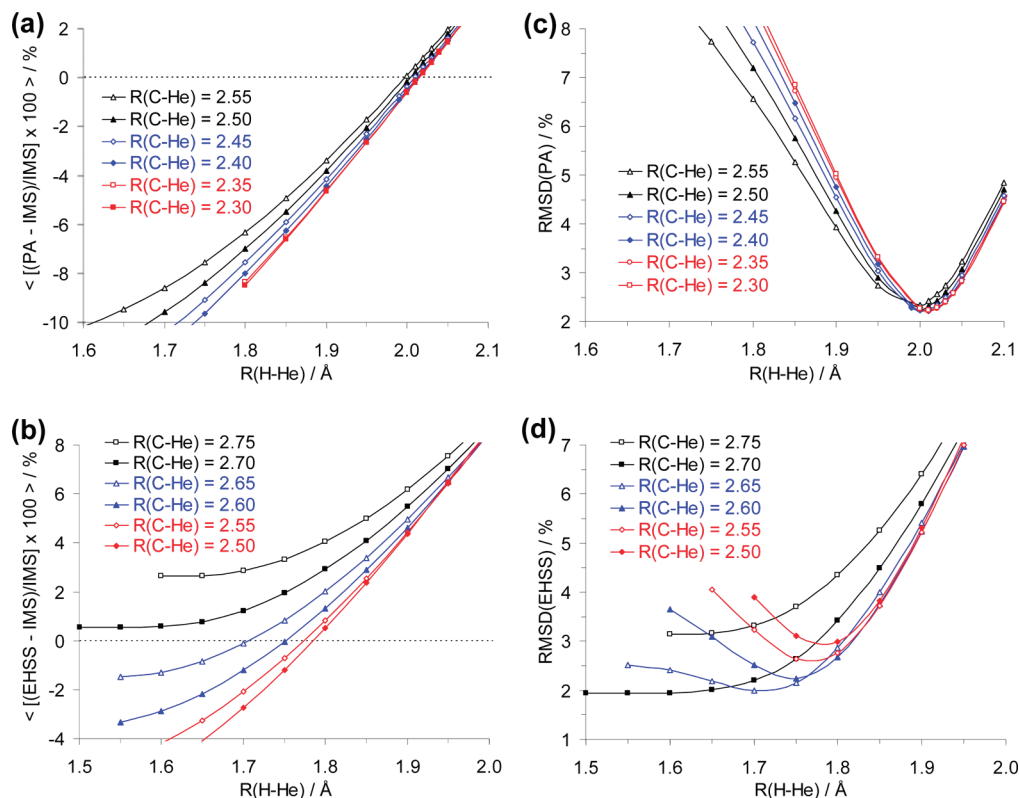


Figure 3. Average percent difference $\langle \% \text{ diff} \rangle = \langle [(\Omega_{\text{THEO}} - \Omega_{\text{IMS}}) / \Omega_{\text{IMS}}] \times 100\% \rangle$ between experimental and theoretical cross sections calculated by (a) the PA model and (b) the EHSS model using different parameters. Each value is the average of calibrants including $\text{TAA-}n$, $[\text{C}_6\text{H}_6]^+$, $[\text{C}_{10}\text{H}_8]^+$, and $[\text{TPP-Fe(III)}]^+$. Root-mean-square deviation (rmsd) values are shown in (c) for the PA model and (d) for the EHSS model.

Supporting Information section (Table S1). The optimal values for the EHSS model are not as clearcut as few sets of parameters give similar rmsd values (Figure 3d); for instance, the rmsd values for the parameters $(R(\text{H-He})/\text{\AA}, R(\text{C-He})/\text{\AA}) = (1.50, 2.70)$, $(1.70, 2.65)$, and $(1.75, 2.60)$ are 1.94%, 1.99%, and 2.24%, respectively. The parameter $R(\text{C-He}) = 2.70 \text{ \AA}$ is chosen based on a DFT-MD simulation at 298 K for C_{60}^{+} ; the average EHSS cross sections of 121.5 \AA^2 for $R(\text{C-He}) = 2.70 \text{ \AA}$, 119.8 \AA^2 for $R(\text{C-He}) = 2.65 \text{ \AA}$, and $117.8 (0.7) \text{ \AA}^2$ for $R(\text{C-He}) = 2.60 \text{ \AA}$ (all with a standard deviation of 0.7 \AA^2) are comparable with our previously measured value of 123 \AA^2 .³⁵ It is interesting to note that, for the PA model, the predicted cross sections are mainly determined by the hydrogen atoms. It is apparent that the multiple scattering effects in the EHSS model can be compensated by the large $R(\text{H-He}) = 2.01 \text{ \AA}$ value optimized for the PA model. For the EHSS model, the optimized $R(\text{C-He})$ is much larger than that of $R(\text{H-He})$ (by 1.20 \AA), a distance longer than the typical C–H bond lengths of $1.0\text{--}1.1 \text{ \AA}$. The large $R(\text{C-He})$ and small $R(\text{H-He})$ reduce the local roughness of a molecular surface, which can overestimate the effects of multiple scattering.⁵ In other words, the theoretical cross sections predicted by the EHSS model using the parameters optimized in this work are solely determined by the carbon atoms. This, of course, means that all hydrogen atoms of a given geometry can now be ignored without changing the resulting predicted cross sections (see Table S2 in the Supporting Information section). This simplification reduces the computational time significantly, and is particularly important when structures of large biomolecules are obtained by means of X-ray crystallography from which the coordinates of hydrogen atoms are not determinable.

Similar optimization procedures for the parameters of nitrogen and oxygen atoms, $R(\text{N-He})$ and $R(\text{O-He})$, were also per-

formed using protonated glycine $[\text{Gly} + \text{H}]^+$ and alanine $[\text{Ala} + \text{H}]^+$, protonated cyclic-dipeptide $[\text{cXxxXxx} + \text{H}]^+$ ($\text{Xxx} = \text{Gly, Ala, Ser, and Val}$) and $[\text{cYyyPro} + \text{H}]^+$ ($\text{Yyy} = \text{Ala and Val}$), and $[\text{hemin}]^+$ as the calibrants. For simplicity, $R(\text{N-He})$ and $R(\text{O-He})$ were treated as equal to each other. The optimal values determined were 2.26 \AA for the PA model and 2.50 \AA for the EHSS model. The cross sections as determined for the various molecules are shown in Table 1. A full list of the numerical data obtained from the models using different parameters is available in the Supporting Information section (Table S3).

With the new sets of parameter, the absolute percent difference of the theoretical cross sections from the experimental cross sections for each calibrant is smaller than 5% (except for $[\text{hemin}]^+$ and $[\text{TPP-Fe(III)}]^+$) with the majority being within 2% (as indicated by the bolded numbers in blue color). The average percent difference $\langle \% \text{ diff} \rangle$ and rmsd of all calibrants are only -0.2% and 2.1% for the PA model and 0.6% and 1.9% for the EHSS model, a significant improvement over the values calculated using the original parameters (Table 1). The one exception is for the cross sections of $[\text{hemin}]^+$ and $[\text{TPP-Fe(III)}]^+$, which were correctly predicted by the original parameters, and are underestimated by 5.5% and 5.6% , respectively, in the PA model with the new set of parameters. This is consistent with the fact that the PA model usually underestimates the cross section of an ion with a concave molecular surface.⁵

Parameters for the Trajectory (TJ) Model. In the TJ model, the scattering angles are determined by propagating classical trajectories between buffer gas atoms and the target ion in an intermolecular potential (eq 3). The potential used comprises two terms: van der Waals and charge-induced dipole interactions. The van der Waals interaction is described by the Lennard-Jones potential, with the depth (ϵ) and distance (σ) of the two-

body 6-12 interaction treated as adjustable parameters. The TJ model is computationally intensive and optimizing the parameters for H, C, N, and O atoms (8 dimensions) is thus impractical. For simplicity, the two sets of parameters in the original MOBCAL program, (1) H atom and (2) C, N, and O atoms, were used and multiplied by a scaling factor (S_{TJ}), which was the adjustable parameter in this work. The charge-induced dipole interaction was evaluated by assuming that the charge of an ion is uniformly delocalized over all atoms. This is justified by the facts that, first, the overall potential contributed by the charge-induced dipole interaction is considerably smaller than that by the van der Waals interaction⁴ and, second, replacing the uniformly distributed charge density with a more accurate distribution obtained by quantum chemical calculations makes significant differences only at low temperatures or for ions with highly asymmetric charge distributions.³⁸ Each TJ simulation comprised 10 complete cycles of integration; each cycle had 500 points in Monte Carlo integration of the impact parameter and orientation, and 20 points in velocity integration, resulting in a total of 100 000 points. As the TJ simulation is very computationally expensive compared to the PA and EHSS methods, a TJ simulation was performed for the geometry only at every 50 DFT-MD step. Each theoretical cross section shown in Table 1 is the average value Ω_{TJ} (with standard deviation SD_{TJ}) of all calculated configurations (i.e., 200–1200).

The Ω_{TJ} and SD_{TJ} as shown in Table 1 are the results obtained using the original parameters ($S_{TJ} = 1.0$) and the optimal parameters ($S_{TJ} = 0.92$). The absolute percent difference of the theoretical cross sections from the experimental collision cross sections for each calibrant is smaller than 5%. The average percent difference and rmsd of all calibrants obtained using $S_{TJ} = 0.92$ are -0.1% and 1.6% , respectively, which are significant improvements over those obtained using $S_{TJ} = 1.0$ (8.4% and 8.5% , respectively). A detailed summary of all scaling factors is available in the Supporting Information section (Table S4).

Conformational Identifications Based on Arrival-Time Distributions. The ion-mobility experiments were conducted by introducing a pulse of ions into the drift tube, before which the velocities of the ions have a Boltzmann distribution and are randomized in all directions. A typical ion-mobility spectrum shows a distribution of times during which the ions arrive at the detector. These arrival-time distributions are modeled using the software ATCAL, courtesy of R. R. Hudgins and M. F. Jarrold. ATCAL calculates the diffusion coefficient, D , from K , via the Einstein equation.¹ Comparing the experimental arrival-time distribution with the theoretical distribution assists in detecting the presence of unresolved components within an ion-mobility peak: when the measured ion-mobility peak is much wider than the theoretical peak, the presence of unresolved structures is indicated.

Tetraalkylammonium Ions. Table 2 shows the full width at half-maxima (fwhm) of the ion-mobility spectra of the TAA- n 's (after the arrival-time domain has been converted to the cross-section domain/ \AA^2). As expected, fwhm increases with increasing molecular size, a trend that is correctly predicted by theoretical modeling. However, the experimental distributions are consistently wider than the theoretical distributions with percent differences between experimental and theoretical fwhm of $\sim 15\text{--}20\%$. Significantly, these percent differences are independent of the length of the alkyl chains; as the smallest TAA-1 $[\text{N}(\text{CH}_3)_4]^+$ has a rigid spherical structure, then the larger TAA- n ions must also exhibit spherical, single conformational behavior. The spatial size is well averaged by the four tetrahedral orientated alkyl chains, although many conformations are

TABLE 2: Full Width at Half-Maxima (fwhm) of the Arrival-Time Distributions (in the Cross Section Domain/ \AA^2) Obtained from Experiments (IMS) and from Theoretical Modeling (THEO)^a

	IMS/ \AA^2	ATCAL modeled values			
		single value ^b / \AA^2	% diff	DFT-MD ^c / \AA^2	% diff
TAA-1	4.9	3.9	-20	4.2	-14
TAA-2	6.4	5.3	-17	5.8	-9
TAA-3	8.8	7.3	-18	7.7	-12
TAA-4	10.8	9.1	-15	9.8	-9
TAA-5 (1)	12.9	11.0	-15	12.0	-7
TAA-5 (2)				12.0	-7
TAA-6	15.3	12.9	-16	13.8	-9
TAA-7 (1)	17.9	14.6	-18	16.1	-10
TAA-7 (2)				17.1	-4
TAA-8	19.6	16.3	-17	18.3	-7
[cGlyGly + H] ⁺	5.3	4.2	-21	4.5	-15
[cAlaAla + H] ⁺	6.5	5.0	-24	5.5	-16
[cSerSer + H] ⁺	6.8	5.4	-20	5.9	-12
[cValVal + H] ⁺	8.0	6.4	-19	7.3	-8
[cAlaPro + H] ⁺	7.1	5.6	-21	5.9	-17
[cValPro + H] ⁺	7.6	6.3	-17	6.7	-11
[GlyGlyGly + H] ⁺ (1)	8.6	6.2	-28	6.9	-20
[GlyGlyGly + H] ⁺ (2)				6.3	-27
[GlyGlyGly + H] ⁺ (3)				6.7	-22
[GlyGlyGly + H] ⁺ (4)				6.5	-24
[AlaAlaAla + H] ⁺ (1)	10.0	7.4	-26	8.3	-17
[AlaAlaAla + H] ⁺ (2)				7.5	-25
[AlaAlaAla + H] ⁺ (3)				8.0	-20
[AlaAlaAla + H] ⁺ (4)				7.8	-22
[BK + 2H] ²⁺ (SB)	19.6	14.5	-26	18.5	-6
[BK + 2H] ²⁺ (IM)				21.3	9

^a Percent difference % diff = $[(\text{fwhm}_{\text{THEO}} - \text{fwhm}_{\text{IMS}})/\text{fwhm}_{\text{IMS}}] \times 100\%$. Theoretical cross sections were determined by means of the EHSS model and with the optimized parameters. ^b Distribution modeled based on a single cross section value determined from the peak position of an IMS spectrum. ^c Distribution modeled based on the cross sections of all geometries obtained from DFT-MD samplings.

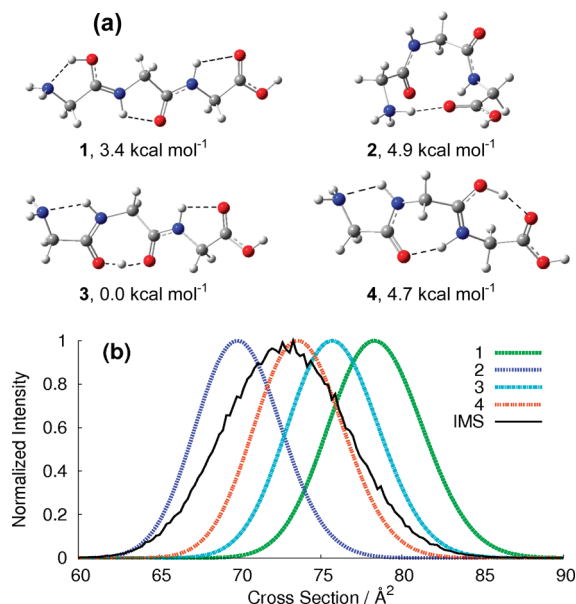


Figure 4. (a) Structures of tautomers of $[\text{GlyGlyGly} + \text{H}]^+$. Relative energies/ kcal mol^{-1} are the average values obtained from geometries sampled by DFT-MD simulations. Cross sections/ \AA^2 are evaluated by the EHSS model using optimal parameters. (b) IMS spectra of $[\text{GlyGlyGly} + \text{H}]^+$; the theoretical spectra were modeled using the ATCAL software.

available in each alkyl chain. The difference between experiments and theory can be rationalized partly by the fact that a

TABLE 3: Cross Sections of Singly Protonated Triglycine [GlyGlyGly + H]⁺, Singly Protonated Trialanine [AlaAlaAla + H]⁺, and Doubly Protonated Bradykinin [BK + 2H]²⁺

	expt	original parameters						optimized parameters							
		$R(\text{H-He}) = 2.20,$ $R(\text{X-He}) = 2.70$				$S_{\text{TJ}} = 1.00$		$R(\text{H-He}) = 2.01,$ $R(\text{C-He}) = 2.35,$ $R(\text{N-He}) = 2.26,$ $R(\text{O-He}) = 2.26$				$R(\text{H-He}) = 1.50,$ $R(\text{C-He}) = 2.70,$ $R(\text{N-He}) = 2.50,$ $R(\text{O-He}) = 2.50$		$S_{\text{TJ}} = 0.92$	
		PA	SD _{PA}	EHSS	SD _{EHSS}	TJ	SD _{TJ}	PA	SD _{PA}	EHSS	SD _{EHSS}	TJ	SD _{TJ}		
[GlyGlyGly + H] ⁺	72 ^c 76 ^d 78 ^e														
B3LYP/6-31++G(d,p)															
1		86.5		90.4		83.6		76.0		77.9		76.2			
2		76.7		80.6		75.3		68.0		69.8		69.2			
3		84.3		88.1		81.5		74.2		75.7		74.3			
4		81.9		86.1		79.9		72.2		73.8		73.1			
DFT-MD ^{d,e}															
1		87.7	0.5	92.1	0.5	84.1	0.7	77.1	0.4	79.1	0.5	76.7	0.8		
2		77.4	0.6	81.4	0.7	76.0	0.7	68.6	0.5	70.5	0.6	69.7	0.7		
3		85.1	0.4	89.2	0.5	82.0	0.7	74.9	0.4	76.4	0.4	74.8	0.6		
4		82.5	0.5	86.8	0.5	80.1	0.7	72.8	0.5	74.2	0.4	73.2	0.7		
[AlaAlaAla + H] ⁺	86 ^c 90 ^e														
B3LYP/6-31++G(d,p)															
1		98.2		105.2		97.3		88.4		92.0		89.7			
2		89.3		95.1		88.1		81.1		82.6		81.5			
3		96.9		103.9		96.4		87.2		90.5		89.0			
4		94.0		101.2		94.3		84.7		87.9		86.8			
DFT-MD ^{a,b}															
1		99.2	0.8	106.5	1.1	97.9	1.1	89.2	0.7	92.6	1.0	90.3	1.0		
2		90.0	0.8	95.9	1.0	88.9	1.0	81.6	0.7	83.2	0.9	82.2	0.9		
3		97.5	0.7	104.6	0.9	96.7	1.0	87.8	0.6	90.7	0.8	87.0	0.9		
4		94.8	0.8	101.7	1.0	94.3	1.0	85.5	0.8	88.2	0.8	89.1	0.9		
[BK + 2H] ²⁺	240 ^f 242 ^g 255 ^h														
B3LYP/6-31++G(d,p)															
SB		245		279		272		232		255		256			
IM		250		284		277		236		259		262			
DFT-MD ^{a,b}															
SB		246	3	281	4	270	5	232	3	255	4	256	4		
IM		266	5	305	5	291	7	250	4	276	5	276	5		

^a Average values of theoretical cross sections obtained from the structures sampled from DFT-MD simulations. ^b Standard deviations of theoretical cross section SD_i obtained from the structures sampled from DFT-MD simulations. ^c This work. ^d Reference 42. ^e Reference 43. ^f Reference 45. ^g Reference 35. ^h Reference 46.

finite time width of ion pulse is applied in the IMS experiments and partly by the dynamics effects of a finite temperature (298 K). The latter are revealed by DFT-MD samplings. The arrival-time distribution is traditionally modeled using a single value for the cross section obtained from the peak position of an IMS spectrum. DFT-MD-based arrival-time distributions are obtained by calculating the distributions using the theoretical cross sections of the individual geometries sampled from DFT-MD simulations, which are then averaged. In Table 2, the fwhms of the DFT-MD-based distributions were calculated using the EHSS cross sections of the DFT-MD-sampled geometries. For each ion in Table 2, the percent difference between experimental and theoretical fwhm, when DFT-MD-based distributions were used, is approximately 6–14% smaller than that when a single value of cross section was used. Similar results were also observed for the cyclic dipeptides, which also have well-defined geometries.

Protonated Triglycine [GlyGlyGly + H]⁺ and Protonated Trialanine [AlaAlaAla + H]⁺. It is interesting to note that in Table 2 the IMS spectrum of [GlyGlyGly + H]⁺ is significantly wider than the theoretical spectrum (by 28%) when a single value of cross section was used for the ATCAL modeling, indicating that multiple conformers exist. The proton on a peptide can locate on different basic sites resulting in different tautomeric structures. Figure 4 shows four tautomers of

[GlyGlyGly + H]⁺: the proton is between the *N*-terminal amino nitrogen and the first amide oxygen in **1**, between the *N*-terminal nitrogen and the C-terminal carboxyl oxygen in **2**, between the first and the second amide oxygens in **3**, and between the second amide oxygen and the C-terminal carboxyl oxygen in **4**. All tautomers have average energies within 5 kcal mol^{−1}, which were evaluated by the DFT-MD simulations. The cross sections were calculated by all three models using both the original and optimized parameters and summarized in Table 3. For all tautomers, the cross sections for the geometries optimized at the B3LYP/6-31++G(d,p) performed by the Gaussian 03 package³⁹ are comparable to those for the geometries obtained from the DFT-MD simulations, indicating that the thermal effects at 298 K are not significant to the cross sections. Similar to the calibrants, the cross sections obtained using the original parameters between the various models are dissimilar and are also significantly larger than the experimental cross section of 72.1 Å². With the new sets of parameter, the cross sections of each tautomer obtained by all three models are similar.

Tautomer **1** is the most extended structure and its predicted cross section ($\Omega_{\text{EHSS}} = 79.1 \text{ Å}^2$) deviates the most from the experimental value ($\Omega_{\text{IMS}} = 72 \text{ Å}^2$) by 9.9%; consequently, this structure is the least likely to predominate in terms of population. Tautomers **2**, **3**, and **4** ($\Omega_{\text{EHSS}} = 70.5$, 76.4, and 74.2 Å², respectively) are better candidates, the deviation between

experimental and theoretical cross sections being -2.1% , 6.1% , and 3.1% , respectively. In addition, the DFT-MD-based arrival-time distributions of tautomer **2**, **3**, and **4**, as summarized in Figure 4b, are considerably narrower than the distribution obtained from IMS experiments by $22\text{--}27\%$ (Table 2). Similar results are observed for $[\text{AlaAlaAla} + \text{H}]^+$; all tautomers have average energies within 5 kcal mol^{-1} and the IMS spectrum is much wider than the theoretical arrival-time distributions of all individual tautomers (Table 2 and Figure S1 in the Supporting Information section). The cross section of the most extended structure tautomer **1** ($\Omega_{\text{EHSS}} = 92.6 \text{ \AA}^2$) deviates the most from the experimental value ($\Omega_{\text{IMS}} = 86 \text{ \AA}^2$) by 7.7% . Tautomers **2**, **3**, and **4** ($\Omega_{\text{EHSS}} = 83.2$, 90.7 , and 88.2 \AA^2 , respectively) are better candidates; the deviation between experimental and theoretical cross sections are -3.3% , 5.5% , and 2.6% , respectively. These results are in agreement with a recent infrared multiple-photon spectroscopic study on the structures of $[\text{GlyGlyGly} + \text{H}]^+$ and $[\text{AlaAlaAla} + \text{H}]^+$: the proton can be located on both the amino nitrogen and the amide oxygens under low-energy conditions.⁴⁰

Doubly Protonated Bradykinin $[\text{BK} + 2\text{H}]^{2+}$. The three-dimensional structures of gaseous polypeptide ions can dictate their fragmentations.⁴¹ Bradykinin (BK), a nonapeptide having the amino acid sequence of Arg-Pro-Gly-Phe-Ser-Pro-Phe-Arg, is one of the most thoroughly studied polypeptides.^{35,44–46} The two Arg residues in the peptide allow BK to be easily doubly protonated during electrospray ionization, giving $[\text{BK} + 2\text{H}]^{2+}$. The narrow arrival-time distribution of $[\text{BK} + 2\text{H}]^{2+}$ suggests that either it is isomerically pure or, more likely, only isomers with very similar cross sections exist (Table 2).

Recent DFT studies²² revealed that the lowest-energy structure of $[\text{BK} + 2\text{H}]^{2+}$ contains a salt bridge (SB), in which the C-terminal carboxylic acid group is deprotonated and solvated by a number of groups including the hydroxy group in the side chain of the Ser residue, the protonated guanidine groups in the side chain of both Arg residues, and the protonated N-terminal amino group. The SB structure of $[\text{BK} + 2\text{H}]^+$ is compact with comparable size to the singly charged $[\text{BK} + \text{H}]^+$.^{35,45} DFT studies have also predicted another class of tautomers of $[\text{BK} + 2\text{H}]^{2+}$ in which the C-terminal carboxylate anion in the SB structure is protonated, giving an ion-molecular (IM) structure with two positive charges formally sequestered at the protonated guanidine groups in the side chains of the two Arg residues. Although the IM structure is relatively flexible with the two formal charges separated far away from each other, the DFT-optimized SB and IM structures are similar in size (Table 3). Table 3 also shows the cross sections calculated using the new parameters optimized in this work. As previously observed, the PA method underestimates the cross sections. For each structure, the cross sections calculated by the EHSS and TJ methods are similar to each other, and both of them are closer to the experimental value and much smaller than those calculated when the original parameters were used.

Interestingly, the SB structure remains compact when the thermal effects at 298 K are included; the cross sections obtained from the optimized structure are almost identical to those from the DFT-MD-sampled structures. Similar results were observed for other compounds, for which thermal effects are insignificant to the cross sections (e.g., atomic clusters⁴⁷ and $[\text{GlyGlyGly} + \text{H}]^+$ and $[\text{AlaAlaAla} + \text{H}]^+$ in Table 3). However, the IM structure is much more flexible and more sensitive to the thermal effects at 298 K ; the IM structures obtained from DFT-MD sampling at 298 K are $14\text{--}17 \text{ \AA}^2$ larger than the optimized structure at 0 K . The significant difference in the thermal effects

on the IM and SB structures of $[\text{BK} + 2\text{H}]^{2+}$ is attributable to their structures: the former is flexible due to Coulombic repulsion between the two protonated arginine residues, while the latter is more rigid because the charges are stabilized by the salt-bridge interactions. Our results are consistent with the results of previous thermodynamics studies;²² the lowest-energy SB structure of $[\text{BK} + 2\text{H}]^{2+}$ exists under low-energy collision conditions.

Conclusions

Ion-mobility experiments have been performed to measure the collision cross sections of 20 selected molecular ions, including tetraalkylammonium ions, protonated cyclic dipeptides, protonated glycine and alanine, benzene radical cation, naphthalene radical cation, iron(III) protoporphyrin IX ion, and iron(III) tetraphenylporphyrin ion. The ion structures were sampled by DFT-MD simulations at a finite temperature of 298 K . Their theoretical cross sections were then calculated by the projection approximation, the exact hard-sphere scattering, and the trajectory models using MOBCAL and EHSSrot softwares. The empirical parameters used in these theoretical models were optimized by comparing the experimental cross sections with the average values obtained from the structures sampled by DFT-MD simulations. The optimal parameters for the PA model are $R(\text{H-He}) = 2.01 \text{ \AA}$, $R(\text{C-He}) = 2.35 \text{ \AA}$, and $R(\text{N-He}) = R(\text{O-He}) = 2.26 \text{ \AA}$; for the EHSS model $R(\text{H-He}) = 1.50 \text{ \AA}$, $R(\text{C-He}) = 2.70 \text{ \AA}$, and $R(\text{N-He}) = R(\text{O-He}) = 2.50 \text{ \AA}$. The large $R(\text{H-He})$ in the PA model compensates for the multiple scattering effects as included in the EHSS model. By contrast, the EHSS model requires a small $R(\text{H-He})$ in order to minimize the effects of local roughness of a molecular surface, which tends to overestimate the calculated cross sections. The coordinates of the hydrogen atoms can also be ignored when the EHSS model is employed. For the TJ model, a scaling factor for the Lennard-Jones parameters as implemented in the original MOBCAL software was applied with the optimal value being $S_{\text{TJ}} = 0.92$. The average percent differences between the experimental and theoretical cross sections and their rmsd's are significantly improved to -0.2% and 2.1% , 0.6% and 1.9% , and -0.1% and 1.6% , respectively, for the PA, EHSS, and TJ models.

The new parameters were applied to other peptide ions, including protonated triglycine, protonated trialanine, and doubly protonated bradykinin. For the first two peptide ions, the proton can locate on the N-terminal amino nitrogen, amide oxygens, or carboxy oxygens, giving structures with slightly different cross sections, as revealed by comparing the arrival-time distribution obtained experimentally and theoretically. For $[\text{BK} + 2\text{H}]^{2+}$, the salt-bridge structure was confirmed to be a compact structure even at a finite temperature of 298 K . The ion-molecular structure does not exist, as its structure is flexible and should give a broad arrival-time distribution, which was not observed in our ion-mobility experiments.

This work demonstrates that the simple, computationally efficient EHSS method in combination with the new parameters determined in this study predicts cross sections of molecular ions as accurately as the more complicated, computationally expensive TJ method. Ion-mobility spectrometry coupled with density functional theory, molecular dynamics simulations, and cross-section calculations using the EHSS model (IMS-DFT-MD-EHSS) is a powerful approach for conformational and structural analyses of molecular ions.

Acknowledgment. The DFT-MD simulations and cross-section calculations were performed on computer facilities

provided by the Shared Hierarchical Academic Research Computing Network (SHARCNET: <http://www.sharcnet.ca>). We thank Dr. M. F. Jarrold, Dr. A. A. Shvartsburg, and Dr. R. R. Hudgins for making available to us the mobility software, MOBCAL, EHSSrot, and ATCAL. Funding from the Natural Sciences and Engineering Research Council (NSERC) and MDS Analytical Technologies is gratefully acknowledged.

Supporting Information Available: A full list of numerical data obtained from the models using different parameters, and a detailed summary of all scaling factors. This material is available free of charge via the Internet at <http://pubs.acs.org>.

References and Notes

- (1) Mason, E. A.; McDaniel, E. W. In *Transport Properties of Ions in Gases*; John Wiley & Sons: New York, 1988.
- (2) Kanu, A. B.; Dwivedi, P.; Tam, M.; Matz, L.; Hill, H. H., Jr. *J. Mass Spectrom.* **2008**, *43*, 1–22.
- (3) von Helden, G.; Hsu, M. T.; Gotts, N.; Bowers, M. T. *J. Phys. Chem.* **1993**, *97*, 8182–8192.
- (4) Mesleh, M. F.; Hunter, J. M.; Shvartsburg, A. A.; Schatz, G. C.; Jarrold, M. F. *J. Phys. Chem.* **1996**, *100*, 16082–16086.
- (5) Shvartsburg, A. A.; Jarrold, M. F. *Chem. Phys. Lett.* **1996**, *261*, 86–91.
- (6) Beitz, T.; Laudien, R.; Lohmannsroben, H. G.; Kallies, B. *J. Phys. Chem. A* **2006**, *110*, 3514–3520.
- (7) Wyttenbach, T.; Witt, M.; Bowers, M. T. *Int. J. Mass Spectrom.* **1999**, *182*, 243–252.
- (8) Wyttenbach, T.; Witt, M.; Bowers, M. T. *J. Am. Chem. Soc.* **2000**, *122*, 3458–3464.
- (9) Wong, R. L.; Williams, E. R.; Counterman, A. E.; Clemmer, D. E. *J. Am. Soc. Mass Spectrom.* **2005**, *16*, 1009–1019.
- (10) Baker, E. S.; Bushnell, J. E.; Weckler, S. R.; Lim, M. D.; Manard, M. J.; Dupuis, N. F.; Ford, P. C.; Bowers, M. T. *J. Am. Chem. Soc.* **2005**, *127*, 18222–18228.
- (11) Siu, C. K.; Guo, Y. Z.; Hopkinson, A. C.; Siu, K. W. M. *J. Phys. Chem. B* **2006**, *110*, 24207–24211.
- (12) Gidden, J.; Wyttenbach, T.; Jackson, A. T.; Scrivens, J. H.; Bowers, M. T. *J. Am. Chem. Soc.* **2000**, *122*, 4692–4699.
- (13) Gidden, J.; Bowers, M. T.; Jackson, A. T.; Scrivens, J. H. *J. Am. Soc. Mass Spectrom.* **2002**, *13*, 499–505.
- (14) Gidden, J.; Bowers, M. T. *J. Phys. Chem. B* **2003**, *107*, 12829.
- (15) Jackson, A. T.; Scrivens, J. H.; Williams, J. P.; Baker, E. S.; Gidden, J.; Bowers, M. T. *Int. J. Mass Spectrom.* **2004**, *238*, 287–297.
- (16) Baker, E. S.; Gidden, J.; Simonsick, W. J.; Grady, M. C.; Bowers, M. T. *Int. J. Mass Spectrom.* **2004**, *238*, 279–286.
- (17) Gidden, J.; Ferzoco, A.; Baker, E. S.; Bowers, M. T. *J. Am. Chem. Soc.* **2004**, *126*, 15132–15140.
- (18) Baker, E. S.; Gidden, J.; Ferzoco, A.; Bowers, M. T. *Phys. Chem. Chem. Phys.* **2004**, *6*, 2786–2795.
- (19) Gidden, J.; Baker, E. S.; Ferzoco, A.; Bowers, M. T. *Int. J. Mass Spectrom.* **2005**, *240*, 183–193.
- (20) Baker, E. S.; Manard, M. J.; Gidden, J.; Bowers, M. T. *J. Phys. Chem. B* **2005**, *109*, 4808–4810.
- (21) Wyttenbach, T.; Bushnell, J. E.; Bowers, M. T. *J. Am. Chem. Soc.* **1998**, *120*, 5098–5103.
- (22) Rodriguez, C. F.; Orlova, G.; Guo, Y. Z.; Li, X. M.; Siu, C. K.; Hopkinson, A. C.; Siu, K. W. M. *J. Phys. Chem. B* **2006**, *110*, 7528–7537.
- (23) Polfer, N. C.; Bohrer, B. C.; Plasencia, M. D.; Paizs, B.; Clemmer, D. E. *J. Phys. Chem. A* **2008**, *112*, 1286–1293.
- (24) Shelimov, K. B.; Clemmer, D. E.; Hudgins, R. R.; Jarrold, M. F. *J. Am. Chem. Soc.* **1997**, *119*, 2240–2248.
- (25) Wu, C.; Murray, M. M.; Bernstein, S. L.; Condron, M. M.; Bitan, G.; Shea, J.; Bowers, M. T. *J. Mol. Biol.* **2009**, *387*, 492–501.
- (26) Kresse, G.; Hafner, J. *Phys. Rev. B* **1993**, *47*, 558–561.
- (27) Kresse, G.; Hafner, J. *Phys. Rev. B* **1994**, *49*, 14251–14269.
- (28) Kresse, G.; Furthmüller, J. *Comput. Mater. Sci.* **1996**, *6*, 15–50.
- (29) Kresse, G.; Furthmüller, J. *Phys. Rev. B* **1996**, *54*, 11169–11186.
- (30) Perdew, J. P.; Burke, K.; Ernzerhof, M. *Phys. Rev. Lett.* **1996**, *77*, 3865–3868.
- (31) Blöchl, P. E. *Phys. Rev. B* **1994**, *50*, 17953–17979.
- (32) Nosé, S. *J. Chem. Phys.* **1984**, *81*, 511–519.
- (33) Jarrold, M. F. Mobcal, website at <http://nano.chem.indiana.edu/Software.html>.
- (34) Shvartsburg, A. A.; Mashkevich, S. V.; Baker, E. S.; Smith, R. D. *J. Phys. Chem. A* **2007**, *111*, 2002–2010.
- (35) Guo, Y. Z.; Wang, J. X.; Javahery, G.; Thomson, B. A.; Siu, K. W. M. *Anal. Chem.* **2005**, *77*, 266–275.
- (36) Guo, Y. Z.; Ling, Y.; Thomson, B. A.; Siu, K. W. M. *J. Am. Soc. Mass Spectrom.* **2005**, *16*, 1787–1794.
- (37) Viidanoja, J.; Sysoev, A.; Adamov, A.; Kotiaho, T. *Rapid Commun. Mass Spectrom.* **2005**, *19*, 3051–3055.
- (38) Shvartsburg, A. A.; Hudgins, R. R.; Dugourd, P.; Jarrold, M. F. *Chem. Soc. Rev.* **2001**, *30*, 26–35.
- (39) Frisch, M. J.; Trucks, G. W.; Schlegel, H. B.; Scuseria, G. E.; Robb, M. A.; Cheeseman, J. R.; Montgomery, J. A., Jr.; Vreven, T.; Kudin, K. N.; Burant, J. C.; Millam, J. M.; Iyengar, S. S.; Tomasi, J.; Barone, V.; Mennucci, B.; Cossi, M.; Scalmani, G.; Rega, N.; Petersson, G. A.; Nakatsuji, H.; Hada, M.; Ehara, M.; Toyota, K.; Fukuda, R.; Hasegawa, J.; Ishida, M.; Nakajima, T.; Honda, Y.; Kitao, O.; Nakai, H.; Klene, M.; Li, X.; Knox, J. E.; Hratchian, H. P.; Cross, J. B.; Bakken, V.; Adamo, C.; Jaramillo, J.; Gomperts, R.; Stratmann, R. E.; Yazyev, O.; Austin, A. J.; Cammi, R.; Pomelli, C.; Ochterski, J. W.; Ayala, P. Y.; Morokuma, K.; Voth, G. A.; Salvador, P.; Dannenberg, J. J.; Zakrzewski, V. G.; Dapprich, S.; Daniels, A. D.; Strain, M. C.; Farkas, O.; Malick, D. K.; Rabuck, A. D.; Raghavachari, K.; Foresman, J. B.; Ortiz, J. V.; Cui, Q.; Baboul, A. G.; Clifford, S.; Cioslowski, J.; Stefanov, B. B.; Liu, G.; Liashenko, A.; Piskorz, P.; Komaromi, I.; Martin, R. L.; Fox, D. J.; Keith, T.; Al-Laham, M. A.; Peng, C. Y.; Nanayakkara, A.; Challacombe, M.; Gill, P. M. W.; Johnson, B.; Chen, W.; Wong, M. W.; Gonzalez, C.; Pople, J. A. *Gaussian 03 Revision D.01*; Gaussian Inc.: Wallingford, CT, 2004.
- (40) Wu, R.; McMahon, T. B. *J. Am. Chem. Soc.* **2007**, *129*, 11312–11313.
- (41) Price, W. D.; Schnier, P. D.; Williams, E. R. *Anal. Chem.* **1996**, *68*, 859–866.
- (42) Wyttenbach, T.; Bushnell, J. E.; Bowers, M. T. *J. Am. Chem. Soc.* **1998**, *120*, 5098–5103.
- (43) Hudgins, R. R.; Mao, Y.; Ratner, M. A.; Jarrold, M. F. *Biophys. J.* **1999**, *76*, 1591–1597.
- (44) Wyttenbach, T.; vonHelden, G.; Bowers, M. T. *J. Am. Chem. Soc.* **1996**, *118*, 8355–8364.
- (45) Counterman, A. E.; Valentine, S. J.; Srebalus, C. A.; Henderson, S. C.; Hoaglund, C. S.; Clemmer, D. E. *J. Am. Soc. Mass Spectrom.* **1998**, *9*, 743–759.
- (46) Gill, A. C.; Jennings, K. R.; Wyttenbach, T.; Bowers, M. T. *Int. J. Mass Spectrom.* **2000**, *195/196*, 685–697.
- (47) Book, L. D.; Xu, C.; Scuseria, G. E. *Chem. Phys. Lett.* **1994**, *222*, 281–286.

JP910858Z